

Tracking stall cell dynamics at high Reynolds numbers

Badoui Hanna ^{*}

CSTB, 11 Rue Henri Picherit, Nantes, 44300, France

Bérengère Podvin [†]

Laboratoire EM2C, CNRS, Centralesupelec, Université Paris-Saclay, 8-10 rue Joliot Curie, 91190 Gif/Yvette

Caroline Braud [‡]

Nantes University, Centrale Nantes, LHEEA UMR 6598, 1, rue de la Noë, 44300, Nantes, FRANCE

The spanwise organization of the flow over a thick airfoil is investigated using surface pressure measurements for a range of angles of attack around maximum lift and high Reynolds numbers $O(10^6)$. Locally strong pressure fluctuations, which are not detected in the global lift coefficient, are shown to be associated with the presence of a stall cell. The stall cell width is of the order of the chord length and increases linearly with the angle of attack, with a weak dependence on the Reynolds number Re_c . Its dynamics at Reynolds numbers larger than 10^6 is dominated by a coherent motion in the spanwise direction with a characteristic velocity of order 0.1 U. The motion can be decomposed into a large-scale, low-frequency sweep with a Strouhal number $St \sim 0.001$ combined with faster, smaller-scale oscillations. The coherence of the stall cell makes it possible to track global dynamics from local measurements.

I. Introduction

Understanding flow behavior in stall conditions is of utmost importance for aerodynamic applications, including aeronautics, turbomachinery, and wind turbines. According to [1], three different types of stall can be identified, depending on the airfoil geometry. These include leading-edge stall for thin airfoils, combined trailing-edge leading edge stall, and trailing edge stalls on thick airfoils. The onset of stall is characterized by complex phenomena such as hysteresis and three-dimensional effects. In particular, [2] and [3] were among the first to provide experimental evidence of a cellular organization of the flow in the spanwise direction. [4] used oil flow visualization to identify mushroom-like or owl-faced structures consisting of counter-swirl patterns on 2D geometries that could not be attributed to end effects. [5] showed that the appearance of stall cells was associated with trailing edge type stalls.

[6] showed that the number of stall cells was found to increase with the wing aspect ratio. Non-integer cell counts were reported and interpreted as evidence of unsteady switching between adjacent integer cell configurations [7] carried out a computational study of a flat plate at low Reynolds number at various angles of attack and found that the spanwise

^{*}PhD student/badoui.hanna@cstb.fr

[†]CNRS researcher/berengere.podvin@centralesupelec.fr

[‡]CNRS researcher/caroline.braud@ec-nantes.fr

aspect ratio of the plate needed to be large enough to observe stall cells. The number of stall cells was also found to increase with the plate aspect ratio. [8] have numerically investigated the formation of stall cells over a NACA 0012 airfoil of a high aspect ratio (10) at high Reynolds number (10^6). They found the presence of stall cell structures over a small range of angle of attack (within 2°), with a spacing of 1.4 to 1.8 chord lengths. [9] determined that the size of the stall cells increases with the angle of attack and with the Reynolds number.

Several models have been proposed for the origin of stall cells. [10] proposed a mechanism in which the three-dimensional structures arose from a Crow-type instability [11] that would deform the two-dimensional separation line. [12] used Prandtl's lifting line theory to derive a model that linked the appearance of stall cells with a negative slope in the lift coefficient with respect to the angle of attack. [13] reached a similar conclusion and derived a formula for the spanwise cell spacing related to that slope. Global stability analysis offers additional insight into the stall cell formation mechanism. [14] provided a theoretical basis for the formation of stall cells using linear stability theory, according to which a stationary three-dimensional global mode consisting of two counter-rotating foci was identified at low Reynolds numbers. Further analyses have been carried out at higher Reynolds numbers combining linear stability analysis with URANS simulations. [15] provided evidence of a non-oscillatory stall global mode for unswept wings. [16] used a similar approach to compute the bifurcation scenario for another 2D airfoil (OA209) and identified a low-frequency oscillation associated with the stall mode.

These theoretical results have been supported by experimental observations. [17] found evidence of a low-frequency oscillation in a range of static stall around maximum lift regime with a Strouhal number based on projected height of the airfoil section and incoming velocity of 0.02. This low frequency oscillation occurred in a narrow region in the early stages of static stall (shallow stall) and was associated with a quasi-periodic switching of the flow between stalled and unstalled conditions. [5] associated the low-frequency instability with thin airfoils. However, [6] showed that stall cell patterns on thick airfoils were responsible for large-amplitude fluctuations occurring at a very low frequency, which was significantly lower than that associated with bluff body vortex shedding. Recently, [18] observed such switches on a 2D thick airfoil at high Reynolds numbers, which they connected with spatial bistability in space between two chords on each side of the airfoil [19]. The bistability phenomenon was further characterized in [19], but the link between bistability and a stall cell could not be confirmed due to the lack of extensive spanwise measurements.

This missing link is provided in the present study, which describes an experimental investigation of the same thick 2D airfoil at high Reynolds numbers based on time-resolved pressure measurements along chords and transverse lines. The connection between global and local pressure fluctuations is examined in detail, allowing identification of a stall cell and tracking of its dynamics. Special attention is given to the highest Reynolds number $Re = 3.4 \cdot 10^6$ which is the closest to wind energy applications. The paper is organized as follows: after a presentation of the experiment, an analysis of pressure statistics is carried out. The main characteristics of the stall cell are then extracted from local measurements. Complementary insight is provided by the application of Proper Orthogonal Decomposition.

II. Set-up

The experimental 2D geometry corresponds to the extruded section of a 2MW commercial wind turbine operated by VALEMO at the Saint-Hilaire de Chaléons site in France. More details on the scan procedure is available in Braud *et al* [20] and the 3D blade shape is available on the AERIS platform [21]. The location of the section is at 80% of the rotor radius. The airfoil is 5 m wide and has a full scale chord length of $c = 1.25m$. Test campaigns were conducted in the aerodynamic test section of the CSTB climatic wind tunnel at Nantes-France (see figure 1) as part of the ANR/SNF MISTERY project. The dimensions of the tunnel are respectively 6 m, 5 m and 12 m for width, height and length. The airfoil has a maximum thickness of 20%, located at 33% of the chord, and a maximum camber of 4%, located approximately at 49% of the chord. Its aspect ratio is 4 and the maximum blockage ratio is 8% when the angle of attack is 24°.

The airfoil is equipped with a total of $N = 476$ pressure taps, located along full chords as well as on transverse lines on the suction side of the airfoil (see figure 2). The pressure taps were connected to five multiplexed EPS pressure scanners of 32 channels each, using 1.5m long vinyl tubes with an internal diameter of 0.8mm. Two pressure sensor ranges were used depending on their location, 0 to 7 kPa near the leading edge suction peak and 0 to 2.5 kPa elsewhere. The precision over the full measurement range was estimated to be $\pm 0.03\%$. The transfer function of the whole system (tubes plus sensor cavity) has been measured off-line at a sampling frequency of 1024Hz (for the methodology, see, e.g., Holmes & Lewis [22] and Whitmore *et al.* [23]). The cut-off frequency is approximately 200Hz. The signal acquisition is performed using two National Instrument acquisition boards linked by real-time system integration for synchronization purposes. During the measurements, the sampling frequency was 512 Hz. During post-processing, the inverse transfer function is applied to the raw signals before the analysis.

The sensor locations presented in figure 2 and 3 are distributed on three chords located at, $y = 0.36c, 0$ and $-0.36c$, denoted respectively as Y_P, Y_0 and Y_M , and on four transverse lines located at $x = 0.2c, 0.4c, 0.55c$ and $0.75c$ denoted respectively as X_1, X_2, X_3 and X_4 . The minimal spacing between the pressure taps is $0.026c$. Four Reynolds numbers based on the incoming velocity and airfoil chord in the range $[5 \times 10^5, 3.4 \times 10^6]$ were investigated.

III. Pressure statistics

A. Global and local loads

Figure 4 compares the global average lift coefficient $\langle C_L \rangle$ obtained from balance measurements with the local lift coefficient obtained from pressure measurements at two crown locations (Y_P and Y_M) on either side of mid-span for $Re_c = 3.4 \times 10^6$. The difference between global and local measurements of $\langle C_L \rangle$ is strongest for $9^\circ \leq AoA(\circ) \leq 12^\circ$ where a localized $\langle C_L \rangle$ peak is observed in the local measurements. This peak is followed by a sharp negative slope over a narrow range of angles of attack, while the global lift keeps increasing more slowly towards a maximum around

$AoA = 18^\circ$ before decreasing slowly. This negative slope, which is also observed by Spalart [12], is a first indication of the presence of stall cells.

The lift coefficient standard deviation is also very different for global and local measurements. Locally, two main fluctuation peaks are present:

- a wide peak for $AoA \in [12^\circ, 15^\circ]$ at the inflection point of $\langle C_L \rangle$, for which the negative slope of the mean lift is maximum,
- a higher one at high $AoA > 24^\circ$ where stall occurs.

This second local peak is similar to that observed in the global lift fluctuations. In contrast, the level of the first local peak is at least twice higher than the global lift fluctuation and only a steady increase is observed in the global measurements for $AoA \in [12^\circ, 15^\circ]$. This indicates that the local, intense load fluctuations are not accounted for in global measurements in that range. The pressure fluctuations in the local measurements were shown to increase progressively in intensity with the Reynolds number (not shown, see[24]), indicating that this local intensity increase is characteristic of high Reynolds numbers.

B. Distribution along lines and chords

This section focuses on the case $AoA = 15^\circ$ and $Re = 3.4 \times 10^6$ that corresponds to the largest fluctuation level. The distribution of the average pressure coefficient along the chord Y_M is shown in figure 5. As discussed in [19], it is characterized by a strong decrease followed by a plateau associated with separation, the origin of which corresponds to the steady separation point, denoted SSP and shown in figure 5. The steady separation point is typically defined as the first point where the pressure gradient becomes sufficiently close to zero (in practice, the criterion $d \langle C_p \rangle / dx < 1$ used in [18] is applied). Beyond the steady separation point, the pressure coefficient remains nearly constant and low in magnitude, and the flow is expected to be fully separated. The pressure coefficient C_p in the separation region may take occasionally higher values due to oscillations of the separated shear layer above the surface, but will remain close to the pressure coefficient C_{P_S} measured at the SSP, with a higher bound $C_{P_{min}} \gtrapprox C_{P_S}$.

This makes it possible to define a chord-based colormap for the pressure coefficient that allows to distinguish attached and separated flow regions. This colormap is represented in figure 5 and is defined as follows:

- If $C_p < C_{P_{min}}$ (grey): the flow is attached.
- If $C_p > C_{P_S}$ (dark pink): the flow is fully separated.
- If $C_{P_{min}} \leq C_p \leq C_{P_S}$ (light pink): the flow is either attached (upstream of the SSP) or separated (downstream of the SSP). Due to the strong pressure gradient upstream of separation, the size of the upstream region is expected to be small and adjacent to the SSP. This intermittent region is actually located within the intermittent separation point peak and always ahead of SSP, as highlighted in [19]. However, because the Separation Point criteria can also be used instantaneously, it is preferred in the colormap representation.

The chord-based colormap can be adapted to the full set of measurements by respectively replacing $C_{P_{min}}$ and C_{P_S} with the minimum of $C_{P_{min}}$ and the maximum of C_{P_S} taken over the three chords Y_i for $i \in \{-, 0, +\}$. These values will be denoted $C_{P_{min}}^m$ and $C_{P_S}^M$. Although perfect correspondence cannot be guaranteed, using this colormap makes it possible to determine regions where the flow is attached (above $C_{P_S}^M$, in grey), fully separated (below $C_{P_{min}}^m$, dark pink), and likely to be separated (between $C_{P_{min}}^m$ and $C_{P_S}^M$, light pink).

Figure 6 shows the time-averaged pressure coefficient for the different transverse lines using this colormap. It can be seen that the flow remains essentially attached at X_2 . Along the transverse line X_2 , the average pressure reaches a maximum in the center region and decreases on each side. However the pressure levels remain low and the flow is expected to remain attached. Similar variations are observed for X_3 but the pressure levels are higher, so that the flow remains attached on the sides, while it is separated in the center region. The pressure distribution along X_4 is similar to that of X_3 in the center region. Moving away from the mid-span $y = 0$, the pressure reaches a local minimum close to the threshold value then increases again on the sides of the airfoil, so that unlike along X_3 , the flow remains almost fully separated along X_4 . This spanwise organization of the pressure fluctuations is similar to that observed by [15] or [25] and is characteristic of the presence of a stall cell.

Figure 7 shows the pressure standard deviation along the lines and chords. Figure 7 left) shows that two maxima are present on each side of each transverse line ($y/c > 0$ and $y/c < 0$), in the range $y/c = \pm 0.5$ for $X_2 = 0.4c$, and $y/c \sim \pm 1$ for $X_3 = 0.55c$ and $X_4 = 0.75c$. The presence of these two maxima indicates regions of high fluctuations, consistent with the intermittent presence of separated flow. The maximum levels at X_2 are similar to those identified for the chords Y_M and Y_P shown in Figure 7 right) - the lower levels for Y_0 are due to a smaller number of pressure taps, see figure 3). The location of the fluctuation maximum, defined as the intermittent separation point by [19], is around $x/c = 0.35$ along the three chords. The location of the fluctuation maxima will be used below to describe the steady wall stall cell footprint.

IV. Stall cell characterization

In this section we investigate the connection between local measurements and the stall cell over the range of angles of attack for which high fluctuation levels are observed. This corresponds to the first peak width of the lift fluctuation, $10^\circ < AoA < 18^\circ$ (see figure 4) and will be referred to as the stall cell regime.

A. Steady features

Pressure statistics such as fluctuation maxima over the chords and transverse lines are first examined to determine the steady footprint of the stall cell. The time-averaged coefficient is represented in Figure 8a) using the same colormap as in figure 6. The locations of local pressure maxima along chords and lines of figure 7 are reported in both plots as green dots. The standard deviation map represented in Figure 8b) shows that the pressure fluctuation levels reach a

global maximum on X_2 in two regions centered around the chords Y_P and Y_M . An outline of the stall cell front was provided by a virtual line interpolating all fluctuation maxima except those of X_4 which are located at the rear of the cell. The interpolation was based on a second-order polynomial for the highest two Reynolds numbers and on a linear fit for the lowest two Reynolds numbers, for reasons that will be detailed below. The resulting intermittent separation line, represented on the plots as a black dashed line, delimits the front of the cell behind which the flow is separated. It will be referred to as the stall cell separation line (SCSL). The stall cell width can then be defined as the maximum spanwise distance between two points on the stall cell separation line.

Figure 9 compares the separation lines for angles of attack in the stall cell regime at different Reynolds numbers. The stall cell width is on the order of c at the onset of stall ($AoA = 12^\circ$) and increases nearly linearly with the angle of attack at a given Reynolds number to reach more than $2c$ at $AoA = 16^\circ$. A small decrease of about 10-20% in the stall cell width can be observed as the Reynolds number increases from 1.7×10^6 to 3.4×10^6 . For the two lower Reynolds numbers $Re = 0.5 \times 10^6$ and $Re = 0.85 \times 10^6$, the location of the maximum on the central chord Y_0 was located on X_3 and not on X_2 , unlike the higher Reynolds numbers. The presence of this kink motivated the use of linear interpolation and appeared to be consistent with a splitting of the stall cell in two. This conjecture is supported by examination of the pressure standard deviation along the transverse lines for $Re_c = 0.5 \times 10^6$, shown in Figure 10. A third maximum at mid-span is observed for all lines, which is consistent with the presence of two stall cells. For the case $Re_c = 0.85 \times 10^6$, the maximum at mid-span was only observed at X_2 , suggesting only a partial splitting (not shown). As stall cells originate from the separated shear layer, this splitting may be explained by the decrease in shear intensity associated with lower Reynolds numbers.

B. Unsteady features

In this section the time-dependent features of the stall cell are examined. Figure 11 shows the spectrogram of C_P for all lines and chords at $AoA = 15^\circ$ and $Re = 3.4 \times 10^6$. In all cases the local pressure fluctuations are characterized by maxima at low frequencies in the range below 1 Hz. The frequencies f appeared to slightly shift for different angles of attack and Reynolds numbers, but no coherent dependence on the angle of attack or the Reynolds number could be identified. The frequencies are made non-dimensional by defining Strouhal numbers St as $St = fc \sin(AoA)/U$ where $c \sin(AoA)$ represents the projected chord area and U the incoming velocity. Several local maxima are present in the range $St \in [10^{-3}, 10^{-2}]$ (this was also observed for other angles of attack and Reynolds numbers), although a clear global maximum at $AoA=15^\circ$ is observed at a very low frequency $St = 0.001$. Remarkably, the location of the spectral maxima lies on the stall cell separation line (local maxima locations are represented with green lines on each plot), which suggests a strong coherence of the stall cell front.

To investigate this coherence in more detail, correlation coefficients between the pressure signals at the local fluctuation maxima are computed and reported in Table 1 for three angles of attack in the stall cell regime at $Re = 3.4$

AoA	$C(Y_P, Y_M)$	$C(X_3^+, X_3^-)$	$C(Y_P, X_3^+)$	$C(Y_M, X_3^-)$
13°	-0.793	-0.285	0.644	0.583
15°	-0.785	-0.238	0.454	0.45
16°	-0.551	-0.31	0.223	0.241

Table 1 Correlation coefficients C between signals taken at local fluctuation maxima along the chords Y_P and Y_M and the transverse line X_3 for $Re_c = 3.4 \times 10^6$ and $AoA = 13^\circ, 15^\circ$ and 16° . The \pm sign refers to the position of the maximum along X_3 . See text for more details.

10^6 . To alleviate notations, $C(A, B)$ in the table represents the correlation coefficient between the fluctuation maximum locations (a.k.a. intermittent separation points) along A and B, where A and B refer to either lines or chords. A suffix \pm is added to determine the maximum position $y > 0$ or $y < 0$ in the case of transverse lines.

The correlation values are strongest at 13° and tend to decrease with the angle of attack. As observed in [19], a strong anti-correlation is present at the respective maxima along Y_P and Y_M . The anticorrelation is still present but weaker for the two maxima along X_3 , which are located closer to the trailing edge. The same trends were reported for X_2 and X_4 (not shown). We note that generally higher correlations (in absolute value) were observed in the case of X_2 . This difference could be attributed to the presence of turbulent fluctuations associated with fully separated flow along X_3 and X_4 , unlike along X_2 . Table 1 also shows that each of the maxima on X_3 is positively correlated with the intermittent separation point on the chord located on the same side of the airfoil. The correlation is maximal at zero time delay between all locations, which confirms the strong coherence of the stall cell dynamics. This coherence is illustrated in figure 12 which shows the evolution of C_P at the intermittent separation points along Y_P and Y_M for $AoA = 15^\circ$ and $Re = 3.4 \times 10^6$. As detailed in [19], the pressure coefficient is bimodal, and switches between a high-value and a low-value state, corresponding to attached and separated flow respectively. Figure 13 shows the instantaneous pressure coefficient map at the two instants indicated in figure 12 and associated with these two states. The colormap is similar to that used in figure 6, with the difference that instantaneous values are used instead of time-averaged values for $C_{P_{min}}^m$ and $C_{P_S}^M$. It can be seen that each state corresponds to an off-center position of the stall cell, and the pressure switches from one chord to the other. This corresponds to a global displacement of the stall cell in the spanwise direction.

V. POD analysis

To investigate in more detail the global motion of the stall cell, Proper Orthogonal Decomposition (POD) [26] was applied to the fluctuating part of the pressure signal for each angle of attack and three Reynolds numbers (0.8×10^6 , 1.7×10^6 , 3.4×10^6). POD provides a decomposition of the spatial autocorrelation tensor into principal directions (aka spatial POD modes) so that the instantaneous fluctuating signal can be expressed as a combination of these modes. The

pressure coefficient at the j -th location and at time t_k can thus be represented as

$$C_{p,j}(t_k) = \langle C_{p,j} \rangle + \sum_{n=1}^{N_{POD}} a_n(t_k) \Phi_{n,j} \quad (1)$$

where $\langle C_{p,j} \rangle$ is the pressure time-average value, $\Phi_{n,j}$ represents the value at position j of the n -th spatial POD mode, and $a_n(t_k)$ is the amplitude of this mode at time t_k . N_{POD} represents the dimension of the spatial autocorrelation and corresponds to the number of pressure taps considered. The modes Φ_n are the eigenmodes of the spatial covariance of the pressure coefficient and are associated with eigenvalues λ_n , each of which represents the contribution of mode n to the total variance. They will be denoted as Φ_n^G if POD is carried out over the full domain ($N_{POD} = N$), and Φ_n^L if POD is limited to a line of measurements. As the spatial modes are normalized, the eigenvalue λ_n is also the variance of the mode amplitudes a_n .

The eigenvalue λ_n of the three most energetic modes is represented in figure 14 a) for all angles of attack at $Re = 3.4 \times 10^6$ and their relative contribution reported in figure 14 b). The non-monotonic variations in the total variance of the pressure observed in the stall cell regime region $[12^\circ, 16^\circ]$ match those in the energy of the first mode. The second mode also reproduces these trends, but to a much weaker extent, while the relative contribution of the third mode tends to decrease in the region $[12^\circ, 16^\circ]$. The relative contribution of the first two modes is largest at these angles of attack, with a value of about 60-70%. This provides a quantitative measure of the strong spatio-temporal organization of the pressure fluctuations in the stall cell regime.

Figure 15 shows the shape of the first two spatial POD modes at the angle of attack 15° and $Re_c = 3.4 \times 10^6$ along the transverse lines. No significant changes in the shape of the modes were observed at other angles of attack (not shown), except for the change in the stall cell width evidenced in figure 9. The dominant mode at X_2 and X_3 is antisymmetric and characterized by a sinusoidal shape with a $2c$ wavelength in the range $-1 < y/c < 1$, with extremal values located on the outer part of the domain at $y/c = \pm 1$. Along X_4 , this fundamental wavelength is still present (same period), but in opposite phase with respect to X_2 and X_3 , and modulated by its harmonic of wavelength c ranging from $-0.5 < y/c < 0.5$. Due to its antisymmetry, the spanwise average of the first mode along X_2 and X_3 is close to zero. This means that the first POD mode makes almost no contribution to the global pressure coefficient, which explains the discrepancy between the local and global pressure fluctuations evidenced in figure 4. The second mode also displays a sinusoidal shape, but is symmetric with respect to the mid-span. Its wavelength c is half that of the first mode for X_2 and X_3 , with two extremal values at $y/c = \pm 1$, and one local extremum of opposite sign at $y/c = 0$. A subharmonic modulation of wavelength $c/2$ is present at X_4 .

To describe the stall cell dynamics, the joint histogram of the two dominant mode amplitudes a_1 and a_2 is represented in Figure 16. Similar histograms were observed for other angles of attack in the stall cell regime at different Reynolds numbers. High values of $|a_1|$ are generally associated with small or negative values of a_2 , corresponding to a region of

high pressure (separated flow) displaying a strong asymmetry on one side of the airfoil. Conversely, the highest values of a_2 are associated with values of $|a_1|$ close to zero, consistent with a high pressure region located at mid-span. These observations are confirmed by a significant correlation coefficient of -0.4 between the absolute value of the amplitude $|a_1|$ and a_2 . This histogram also shows that some states (i.e. stall cell positions) are more visited than others, which suggests complex, intermittent dynamics.

To investigate the respective action of the modes, Figure 17 shows three POD-based reconstructions of the pressure coefficient C_p^α on the transverse lines X_2 , X_3 and X_4 . The reconstructed pressure coefficients are defined as $C_p^\alpha = a_1^\alpha \phi_1 + a_2^\alpha \phi_2$ for three states of (a_1^α, a_2^α) where $\alpha \in \{-, 0, +\}$. These values correspond to $(a_1^\pm, a_2^\pm) = (\pm\sqrt{\lambda_1}, 0)$ and $(a_1^0, a_2^0) = (0, \sqrt{\lambda_2})$ and are indicated in Figure 16. It can be seen that the main difference between all three states is the spanwise position of the stall cell, although some mild deformation of the cell is also observed. A switch of the stall cell from $y < 0$ to $y > 0$ (from C_p^- to C_p^+) corresponds to a change in the sign of the amplitude of the first mode (from positive to negative). When the amplitude of the first mode reaches zero, the amplitude of the second mode will typically be positive, which means that the stall cell is located at the middle of the airfoil (C_p^0). As the stall cell moves towards $y > 0$, the amplitude a_1 becomes more negative and a_2 decreases. An illustration of the scenario described above is shown in figure 18, which represents the time evolution of the first two normalized POD amplitudes $\tilde{a}_n = a_n / \sqrt{\lambda_n}$, $n = 1, 2$, corresponding to two back-to-back spanwise sweeps over a period of 12 s.

The spectrum of the reconstructed pressure coefficient limited to the first mode is shown in figure 19. The good agreement between figure 19 and figure 11 shows that the low-frequency dynamics, and in particular the maximum observed at $St = 0.001$, are well captured by the first mode, which characterizes the large-scale motion of the stall cell in the spanwise direction. It can be noted that this frequency corresponds to the characteristic time over which the stall cell moves from one side of the airfoil to the other (as seen in figure 18).

To determine whether these global flow dynamics can be tracked through limited measurements, Figure 20 compares the trace of the global modes Φ_n^G with local modes Φ_n^L , which were obtained by independent application of POD on individual transverse lines. It can be seen that the first two modes are largely similar for local and global decompositions on all transverse lines, particularly at X_3 (which corresponds to the position of the steady separation point for this angle of attack, as can be seen in figure 5). This confirms that the pressure fluctuations are globally coherent over the airfoil span. It also suggests that the dynamics of the stall cell can be efficiently tracked through a single transverse line of measurements.

In all that follows we will consider local POD modes computed over the X_2 line, which corresponds to the region of maximum fluctuations. For each mode n , a characteristic frequency f_n for mode n can be computed as

$$f_n = \frac{\int f |\hat{a}_n(f)|^2 df}{\int |\hat{a}_n(f)|^2 df}, \quad (2)$$

where $\hat{a}_n(f)$ is the Fourier transform of the POD mode amplitude a_n . The nondimensional characteristic frequencies for the first two dominant modes are shown in figure 21 at all angles of attack and three Reynolds numbers $\{0.8 \times 10^6, 1.7 \times 10^6, 3.4 \times 10^6\}$. It should be noted that the Strouhal numbers based on f_n are larger than that corresponding to the most energetic frequency since they integrate the effect of all frequencies. A difference can be observed between the lowest Reynolds number and the two higher ones. The characteristic frequencies are significantly higher at $Re = 0.85 \times 10^6$ and show a local minimum in the stall cell regime. In contrast, for the higher Reynolds numbers, the Strouhal numbers are relatively constant around respective values of 0.005 and 0.01 for the first and second POD modes. As a crude approximation, if we assume that $\phi_n(y) \approx e^{ik_n y} + C.C.$ (where *C.C.* represents the complex conjugate) and $a_n(t) \approx e^{-i f_n t} + C.C.$, this defines a phase velocity for each mode $U_n = f_n/k_n$. Since the frequency ratio f_2/f_1 between the modes roughly corresponds to that of their spatial wavenumbers k_2/k_1 , this means that the phase velocity of the first two modes is about the same, which corresponds to a global translation of the stall cell at speed U_c , as $C_p(y, t) = \sum_n a_n(t) \phi_n(y) \approx f(y - U_c t)$. An estimate for the global convection speed U_c of the stall cell can then be given by $U_c \sim 0.1U$. Results at Reynolds numbers larger than 10^6 are therefore consistent with the superposition of a low-frequency sweep and faster, small-scale oscillations, as illustrated in figure 18.

VI. Conclusion

Time-resolved pressure measurements were taken along the chords and span of a moderately thick 2D airfoil at high Reynolds numbers in the range $[0.5, 3.4] \times 10^6$. Evidence of a stall cell is found in a range of angle of attacks $[12^\circ, 16^\circ]$ which is close to the lift maximum and where local loads exhibit a negative slope. The steady footprint of the stall cell can be outlined using a separation line based on local fluctuation pressure maxima. The stall cell width defined from the separation line is found to increase roughly linearly with the angle of attack. It tends to slightly decrease with the Reynolds number for $Re_c > 10^6$. At the two lowest Reynolds numbers $Re_c \leq 10^6$, the cell observed at the higher Reynolds numbers appears to split in two smaller cells. Fluctuations on the separation line are dominated by a range of frequencies lower than 1 Hz and correspond to a motion that is predominantly in the spanwise direction. The stall cell motion can be decomposed into a low-frequency, large-scale sweep with a Strouhal number of order $O(10^{-3})$, and faster, smaller-scale oscillations. It is characterized by a global convection velocity of order $0.1U$.

The results of the study have direct implications for the applications: firstly, stall cell characteristics, such as the frequencies and fluctuation levels measured in the region directly upstream of separation, depend on the Reynolds number, which shows the importance of carrying out large-scale experiments. Secondly, the global dynamics of the stall cell can be tracked from local measurements taken along a transverse line, which opens up interesting possibilities for flow estimation from sparse sensor data and real-time control.

VII. Acknowledgements

This research was performed within the French-Swiss project MISTERY funded by the French National Research Agency (ANR PRCI grant no. 266157) and the Swiss National Science Foundation (grant no. 200021L 21271)

References

- [1] McCullough, G., and Gault, D., “Examples of three representative types of airfoil-section stall at low speed,” *Tech. Rep. NASA-TN-2502*, NASA, 1951.
- [2] Moss, G., and Murdin, P., “Two-Dimensional Low-Speed Tunnel Tests on the NACA 0012 Section Including Measurements Made During Pitching Oscillations at the Stall,” *Tech. rep., TR 68104*, 1968.
- [3] Gregory, N., Quincey, V., Reilly, C. O., and Hall, D., “Progress Report on Observations of Three-Dimensional Flow Patterns Obtained During Stall Development on Airfoils and on the Problems of Measuring Two-Dimensional Characteristics,” *Tech. rep., R.A.E, Farnborough*, 1971.
- [4] Winkelman, A., and Barlow, J., “Flowfield model for a rectangular planform wing beyond stall.” *AIAA Journal*, Vol. 18, No. 8, 1980, pp. 1006–1008.
- [5] Broeren, A., and Bragg, M., “Spanwise variation in the unsteady stalling flowfields of two-dimensional airfoil models,” *39th Aerospace Sciences Meeting and Exhibit*, Reno,NV,USA, 2001.
- [6] Yon, S. A., and Katz, J., “Study of the Unsteady Flow Features on a Stalled Wing,” *AIAA Journal*, Vol. 36, No. 3, 1998, pp. 305–312. <https://doi.org/10.2514/2.372>.
- [7] Taira, K., and Colonius, T., “Three-dimensional flows around low-aspect-ratio flat-plate wings at low Reynolds numbers,” *Journal of Fluid Mechanics*, Vol. 623, 2009, p. 187–207. <https://doi.org/10.1017/S0022112008005314>.
- [8] Manni, L., Nishino, T., and Delafin, P.-L., “Numerical study of airfoil stall cells using a very wide computational domain,” *Computers & Fluids*, Vol. 140, 2016, pp. 260–269. <https://doi.org/https://doi.org/10.1016/j.compfluid.2016.09.023>, URL <https://www.sciencedirect.com/science/article/pii/S0045793016302894>.
- [9] Manolesos, M., Papadakis, G., and Voutsinas, S. G., “Experimental and computational analysis of stall cells on rectangular wings,” *Wind Energy*, Vol. 17, 2014, p. 939–955. <https://doi.org/10.1002/we.1609>.
- [10] Weihs, D., and Katz, J., “Cellular patterns in poststall flow over unswept wings,” *AIAA Journal*, Vol. 21, No. 12, 1983, pp. 1757–1759. <https://doi.org/10.2514/3.8321>.
- [11] Crow, S. C., “Stability theory for a pair of trailing vortices,” *AIAA Journal*, Vol. 8, No. 12, 1970, pp. 2172–2179. <https://doi.org/10.2514/3.6083>.
- [12] Spalart, P. R., “Prediction of Lift Cells for Stalling Wings by Lifting-Line Theory,” *AIAA Journal*, Vol. 52, No. 8, 2014, pp. 1817–1821.

[13] Gross, A., Fasel, H. F., and Gaster, M., “Criterion for Spanwise Spacing of Stall Cells,” *AIAA Journal*, Vol. 53, No. 1, 2015, pp. 272–274.

[14] Rodriguez, D., and Theofilis, V., “On the birth of stall cells on airfoils.” *Theor. Comput. Fluid Dyn.*, Vol. 25, 2011, p. 105–117.

[15] Plante, F., Dandois, J., Beneddine, S., Laurendeau, E., and Sipp, D., “Link between subsonic stall and transonic buffet on swept and unswept wings: from global stability analysis to nonlinear dynamics,” *Journal of Fluid Mechanics*, Vol. 908, 2021, p. A16. <https://doi.org/10.1017/jfm.2020.848>.

[16] Busquet, D., Marquet, O., Richez, F., Juniper, M., and Sipp, D., “Bifurcation scenario for a two-dimensional static airfoil exhibiting trailing edge stall,” *Journal of Fluid Mechanics*, Vol. 928, 2021, p. A3. <https://doi.org/10.1017/jfm.2021.767>.

[17] Zaman, K. B. M. Q., Mckinzie, D. J., and Rumsey, C. L., “A natural low-frequency oscillation of the flow over an airfoil near stalling conditions,” *Journal of Fluid Mechanics*, Vol. 202, 1989, p. 403–442. <https://doi.org/10.1017/S0022112089001230>.

[18] Neunaber, I., Danbon, F., Soulier, A., Voisin, D., Guilmeneau, E., Delpech, P., Courtine, S., Taymans, C., and Braud, C., “Wind tunnel study on natural instability of the normal force on a full-scale wind turbine blade section at Reynolds number $4.7 \cdot 10^6$,” *Wind Energy*, 2022, p. 1-11. [https://doi.org/https://doi.org/10.1002/we.2732](https://doi.org/10.1002/we.2732).

[19] Braud, C., Podvin, B., and Deparday, J., “Study of the wall pressure variations on the stall inception of a thick cambered profile at high Reynolds number,” *Phys. Rev. Fluids*, Vol. 9, 2024, p. 014605. <https://doi.org/10.1103/PhysRevFluids.9.014605>, URL <https://link.aps.org/doi/10.1103/PhysRevFluids.9.014605>.

[20] Braud, C., Keravec, P., Neunaber, I., Aubrun, S., Attié, J.-L., Durand, P., Ricaud, P., Georgis, J.-F., Leclerc, E., Mourre, L., and Taymans, C., “A 3-year database of atmospheric measurements combined with associated operating parameters from a wind farm of 2 MW turbines including rotor geometry,” *Wind Energy Science*, Vol. 10, No. 9, 2025, pp. 1929–1942. <https://doi.org/10.5194/wes-10-1929-2025>, URL <https://wes.copernicus.org/articles/10/1929/2025/>.

[21] Braud, C., and Taymans, C., “2MW Wind Turbine Blade Geometry. [dataset]. Aeris,” , 2024. <https://doi.org/10.5194/wes-10-1929-2025>.

[22] Holmes, J. D., and Lewis, R. E., “The dynamic response of Pressure-Measurement Systems,” 9th Australasian Fluid Mechanics Conference, Auckland, 1986.

[23] Whitmore, S. A., Petersen, B. J., and Scott, D. D., “A Dynamic Response Model for Pressure Sensors in Continuum and High Knudsen Number Flows with Large Temperature Gradients,” Tech. Rep. Technical Memorandum 4728, NASA, 1996.

[24] Hanna, B., Braud, C., Podvin, B., and Deparday, J., “Reynolds effects on wall pressure fluctuations at stall inception of a wind turbine blade section,” *Journal of Physics*, 2024.

[25] Mishra, R., “Wind inflow customisation at wind turbine blade scale using wind tunnel experiments and CFD simulations,” Ph.D. thesis, Ecole Centrale-Nantes, 2024.

[26] Lumley, J., "The structure of inhomogeneous turbulent flows," *Atmospheric Turbulence and Radio Wave Propagation*, edited by A. Iaglom and V. Tatarski, Nauka, Moscow, 1967, pp. 221–227.

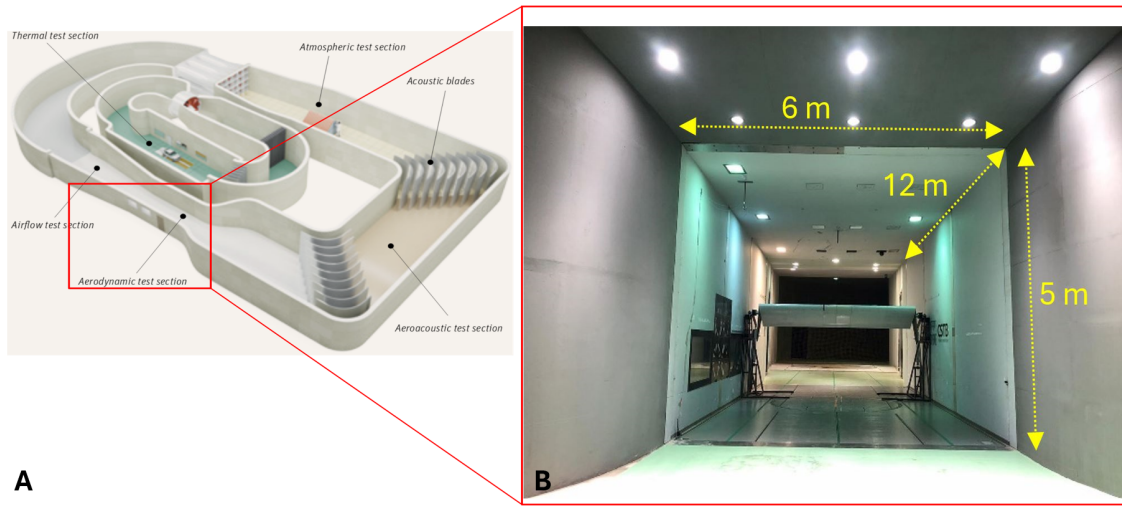


Fig. 1 Aerodynamic test section of the CSTB wind tunnel.

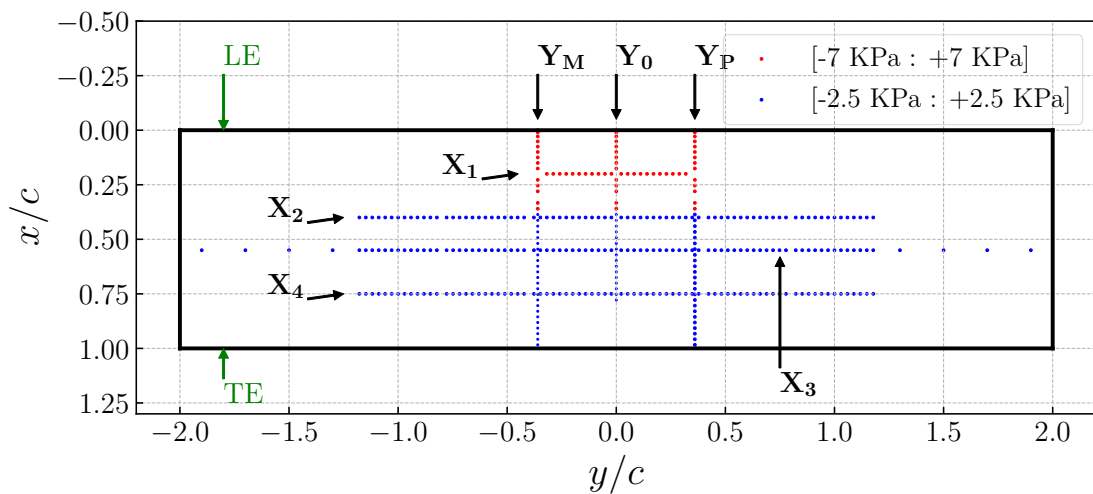


Fig. 2 Pressure tap positions - top view.

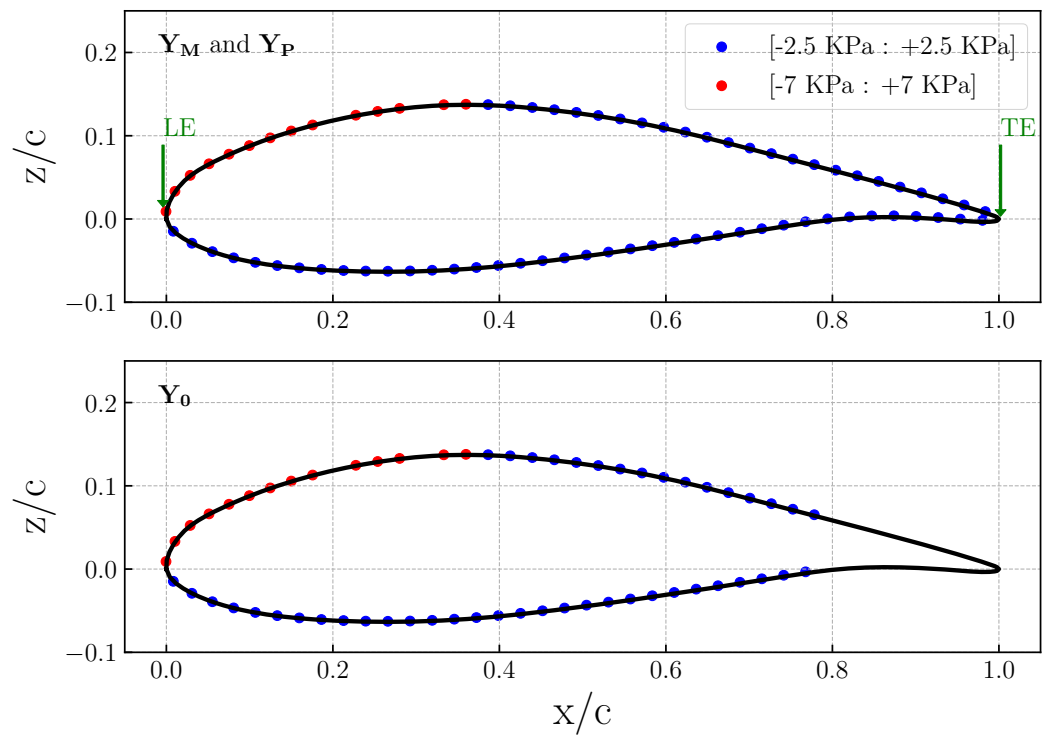


Fig. 3 Pressure tap positions along the chords.

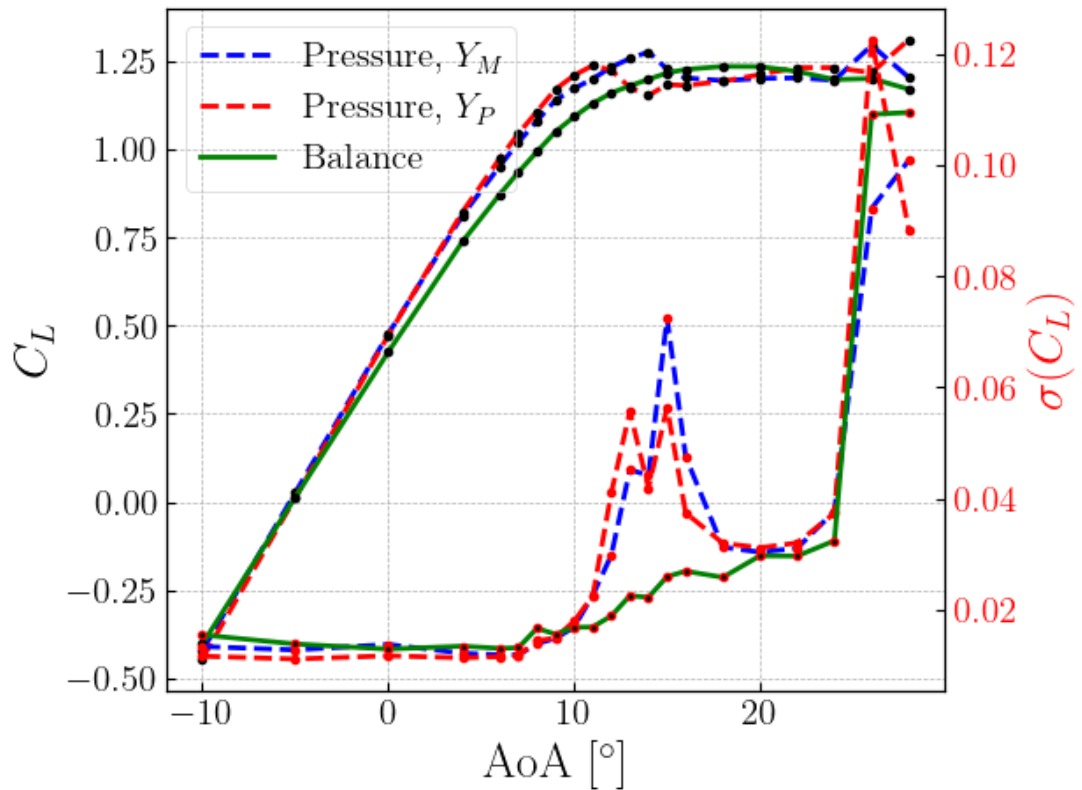


Fig. 4 Time-averaged (black points) and standard deviation (red points) of C_L from the balance (green) and the integration of pressure taps around mid-chord (dash-blue and dash-red lines), Y_M and Y_P for $Re = 3.4 \times 10^6$.

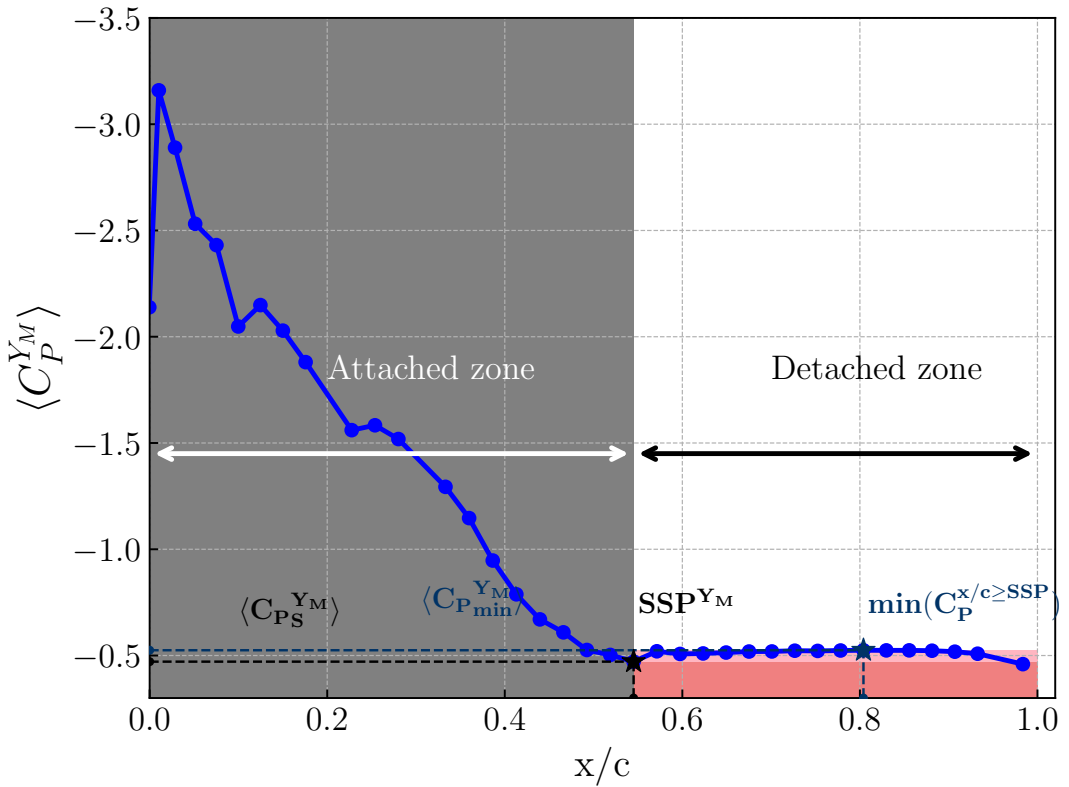


Fig. 5 Mean pressure distribution along the chord on the suction side of the airfoil Y_M at $AoA = 15^\circ$ and $Re = 3.4 \times 10^6$. The colormap based on $C_{P_{min}}$ and C_{P_S} where is defined in the text.

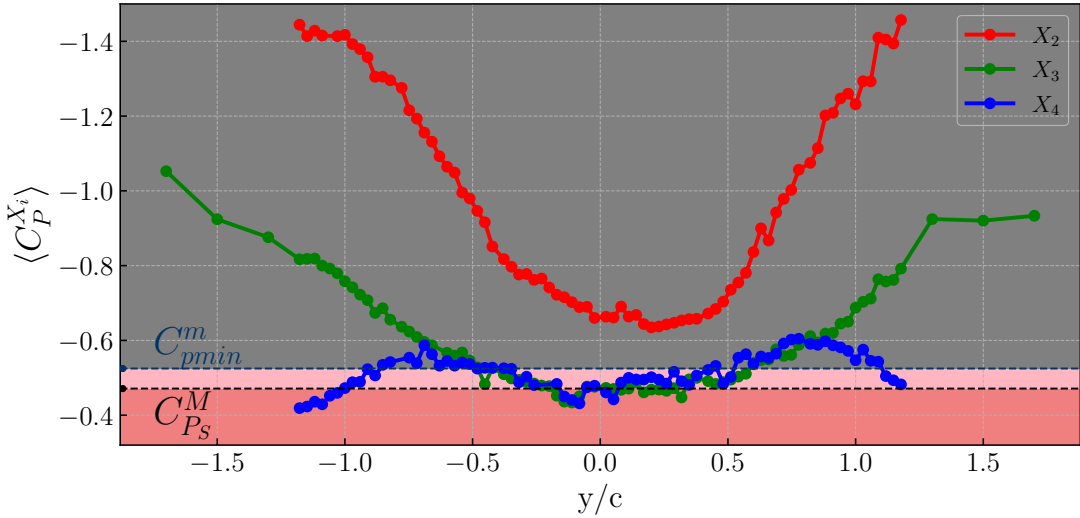


Fig. 6 Mean pressure distribution along the transverse lines at $AoA = 15^\circ$ and $Re = 3.4 \times 10^6$. The colormap based on $C_{P_{min}}^m = \text{Min}_{Y_i} C_{P_{min}}^{Y_i}$ and $C_{P_S}^M = \text{Max}_{Y_i} C_{P_S}^{Y_i}$ where $i \in \{-, 0, +\}$ is defined in the text.

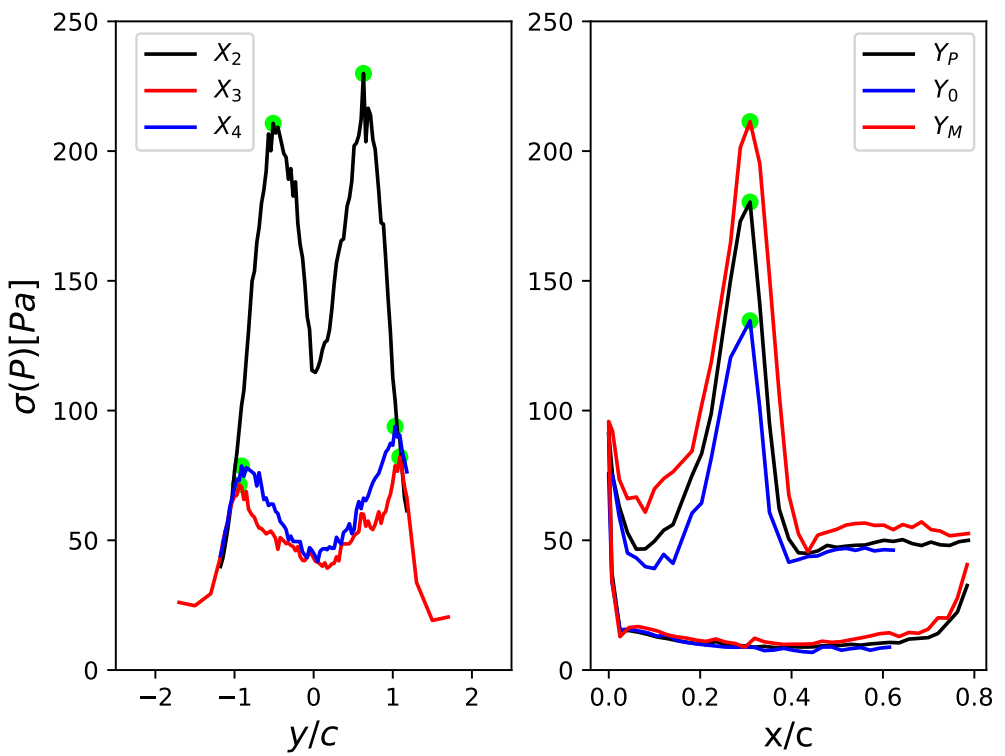


Fig. 7 Peaks of pressure standard deviation along lines (left) and chords (right), at $AoA = 15^\circ$ and $Re = 3.4 \times 10^6$. Green dots are maxima locations of ISP peaks.

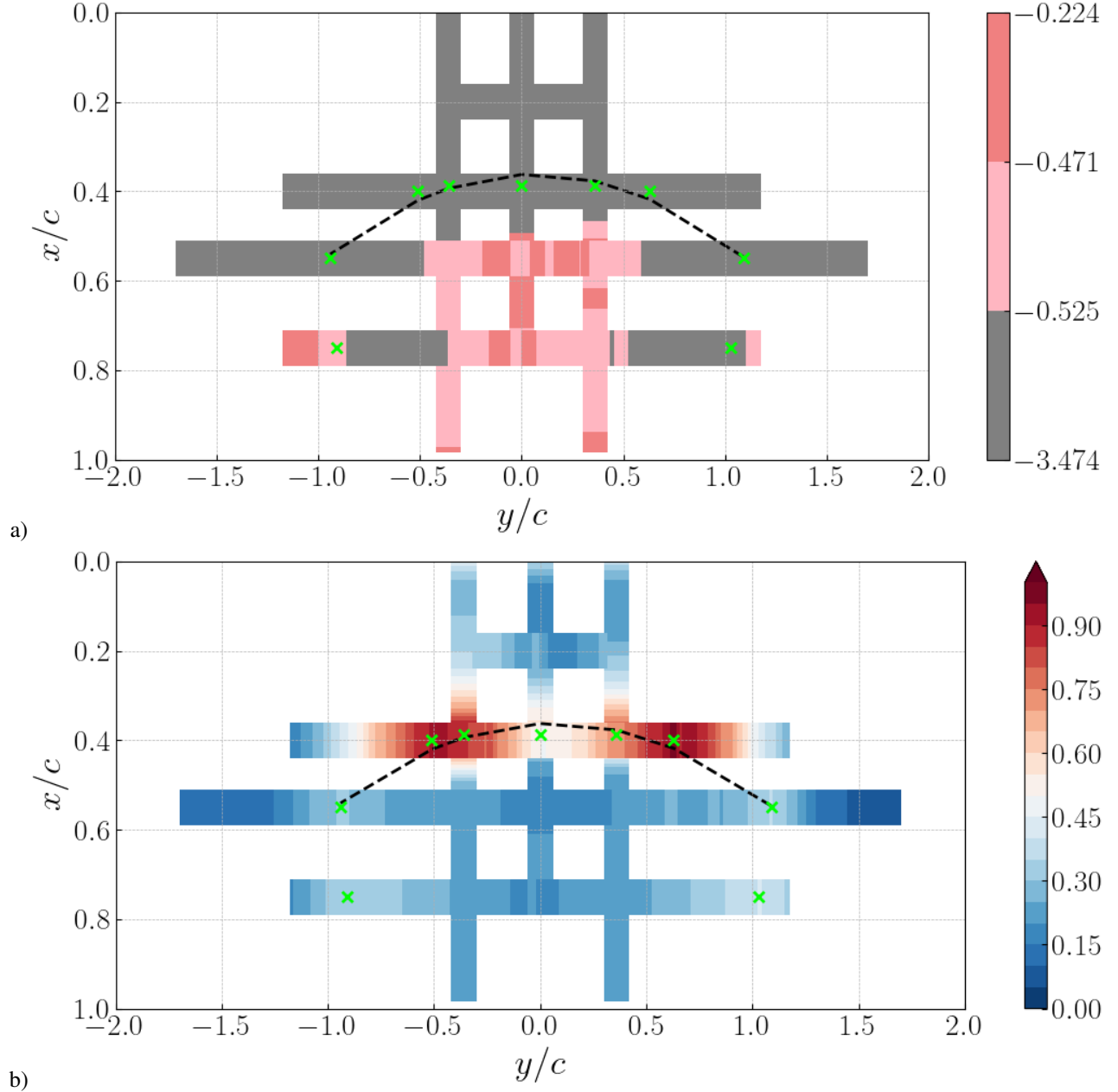


Fig. 8 Stall cell characterization at $AoA = 15^\circ$ and $Re = 3.4 \times 10^6$: a) Mean pressure coefficient, $\langle C_p \rangle$, and b) normalized standard deviation of pressure, $\sigma(P) / \max[\sigma(P)]$. The pink and gray colors of $\langle C_p \rangle$ corresponds to the separation and attached flow region respectively. The black dashed line is obtained by joining the local maxima (green dots) along the three first lines and chords.

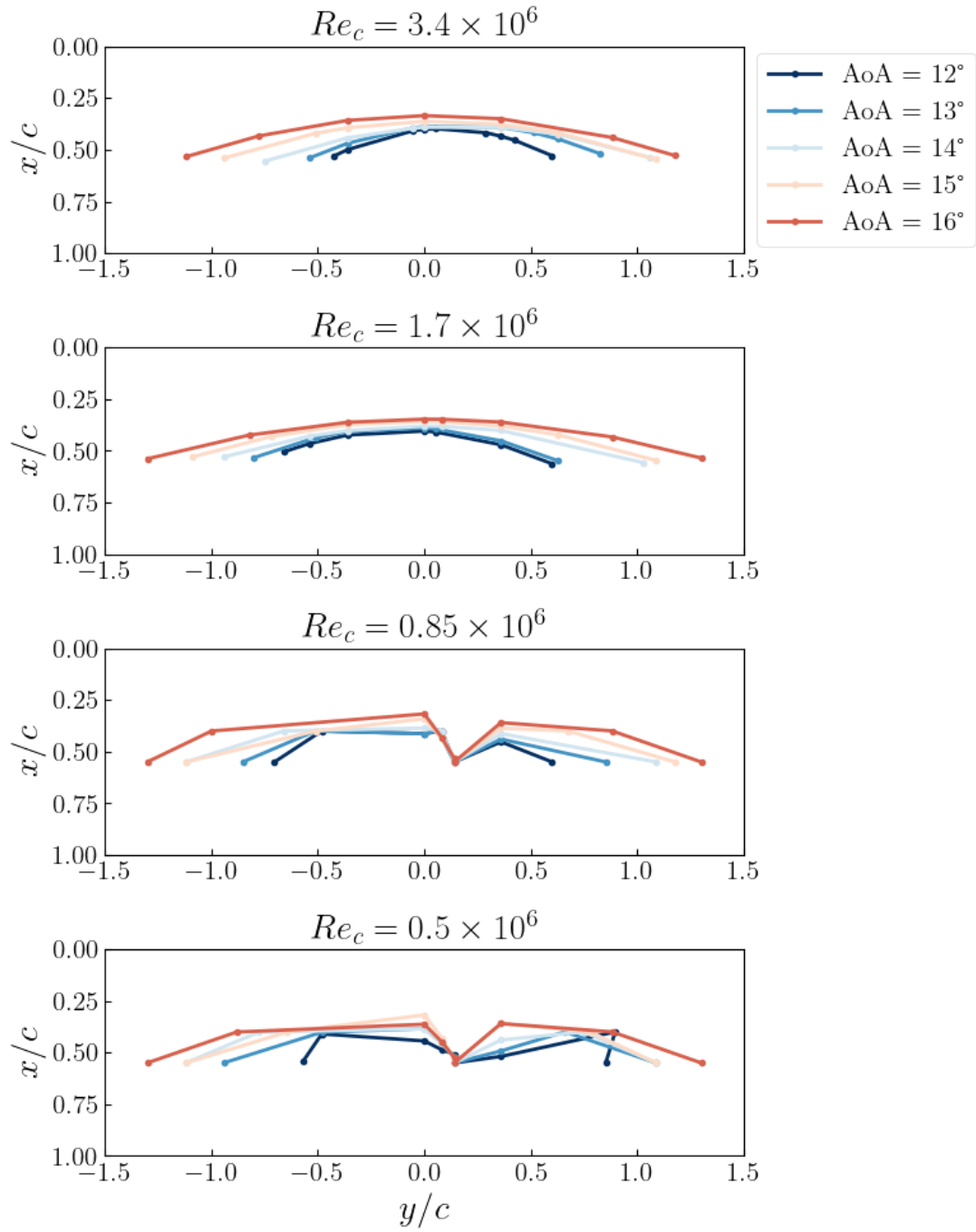


Fig. 9 Evolution of the stall cell front line with AoA for different Reynolds numbers.

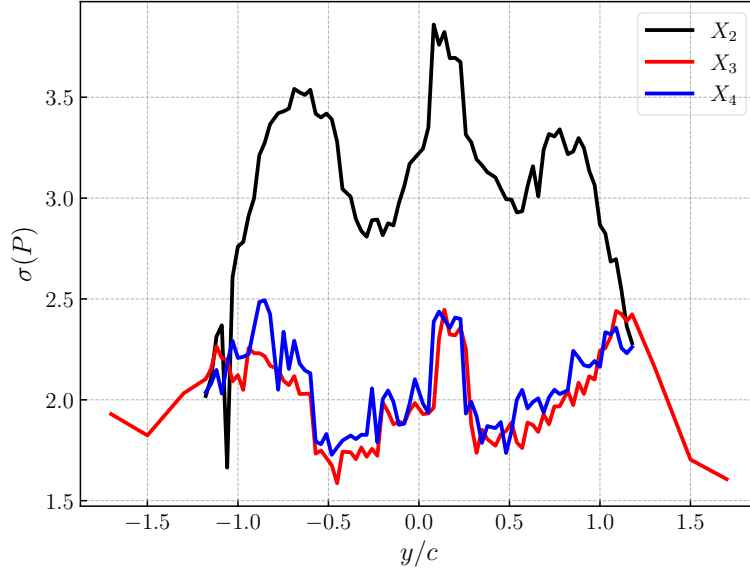


Fig. 10 Peaks of pressure standard deviation along lines at $AoA = 15^\circ$ and $Re = 0.5 \times 10^6$.

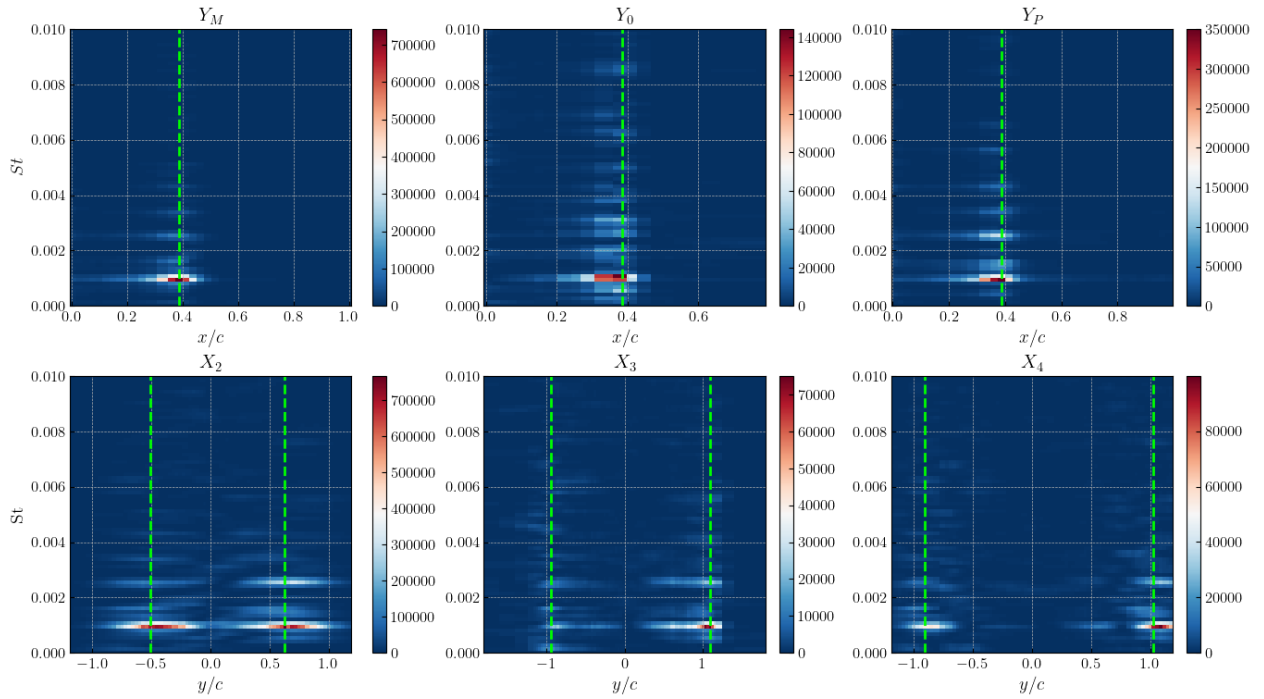


Fig. 11 Spectrogram of C_p at $AoA = 15^\circ$ and $Re = 3.4 \times 10^6$. Green dotted lines corresponds to maxima of $\sigma(P)$ from dotted green points of figure 7.

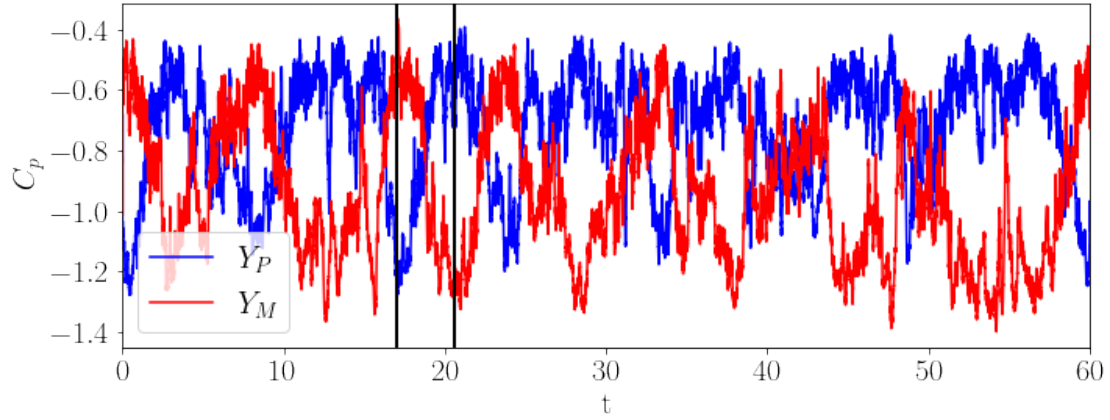


Fig. 12 Evolution of the pressure coefficient measured at the intermittent separation point (maximum fluctuation location) along Y_P and Y_M at $Re = 3.4 \times 10^6$ and $AoA = 15^\circ$. The vertical lines correspond to the instants in figure 13.

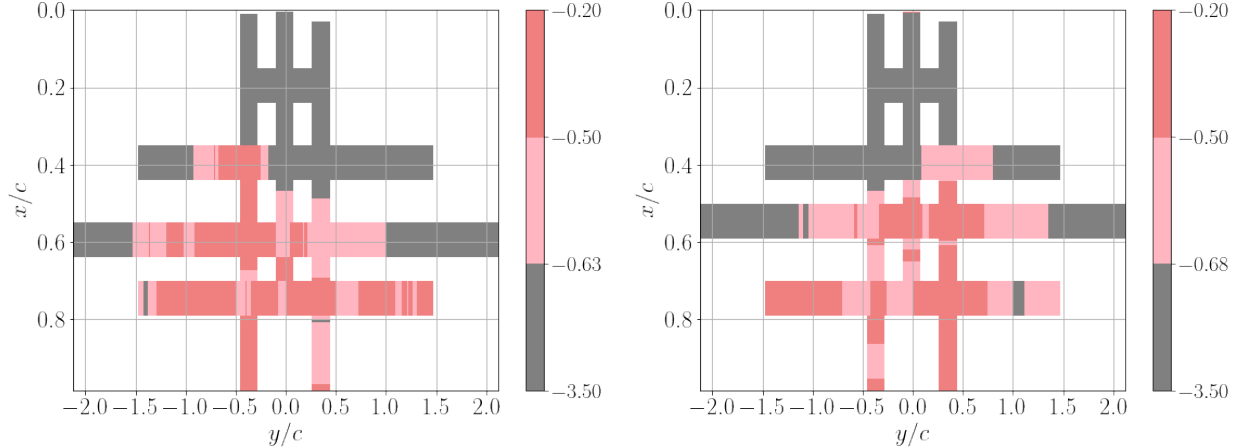


Fig. 13 Pressure coefficient at instants $t = 17.03$ and $t = 20.60$ corresponding to the vertical black lines in figure 12. The dashed lines are obtained by interpolation of the pressure fluctuation maxima along the chords and transverse lines X_2 and X_3 as in figure 8

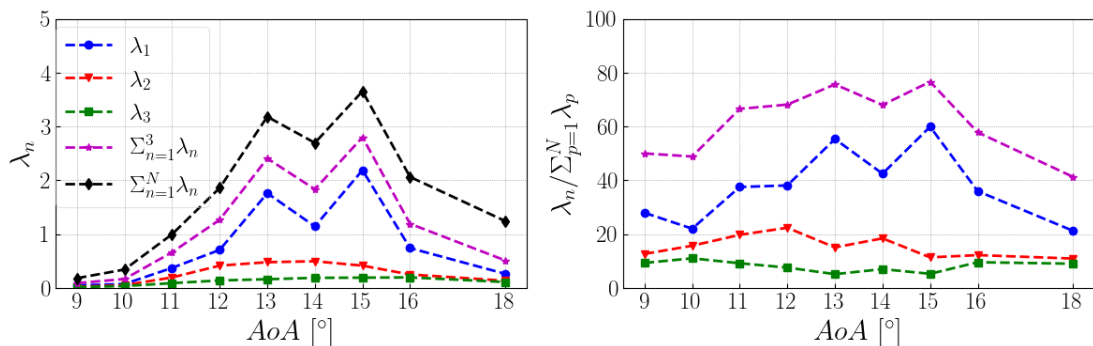


Fig. 14 Global POD spectra at $Re = 3.4 \times 10^6$ for the different angles of attack. a) Eigenvalues λ_n) Relative contribution of the eigenvalues.

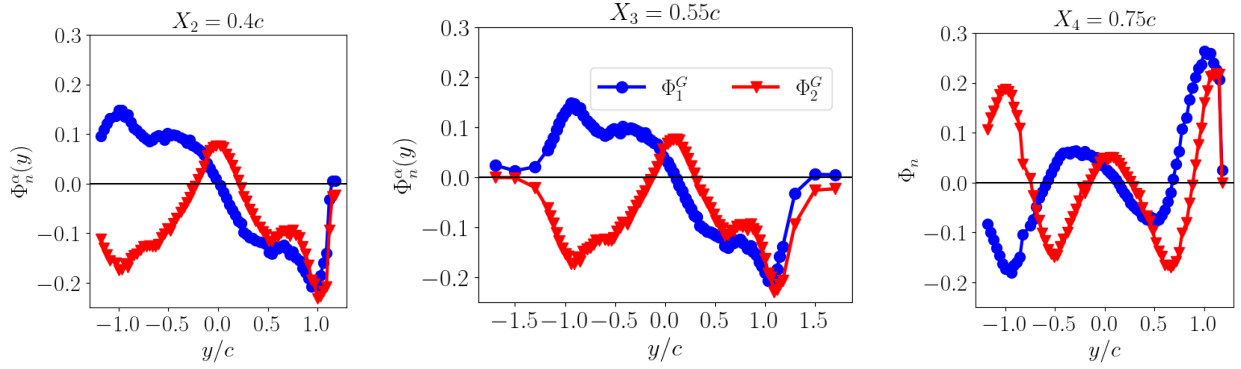


Fig. 15 POD spatial modes (defined over the full domain) at $AoA = 15^\circ$ and $Re_c = 3.4 \times 10^6$.

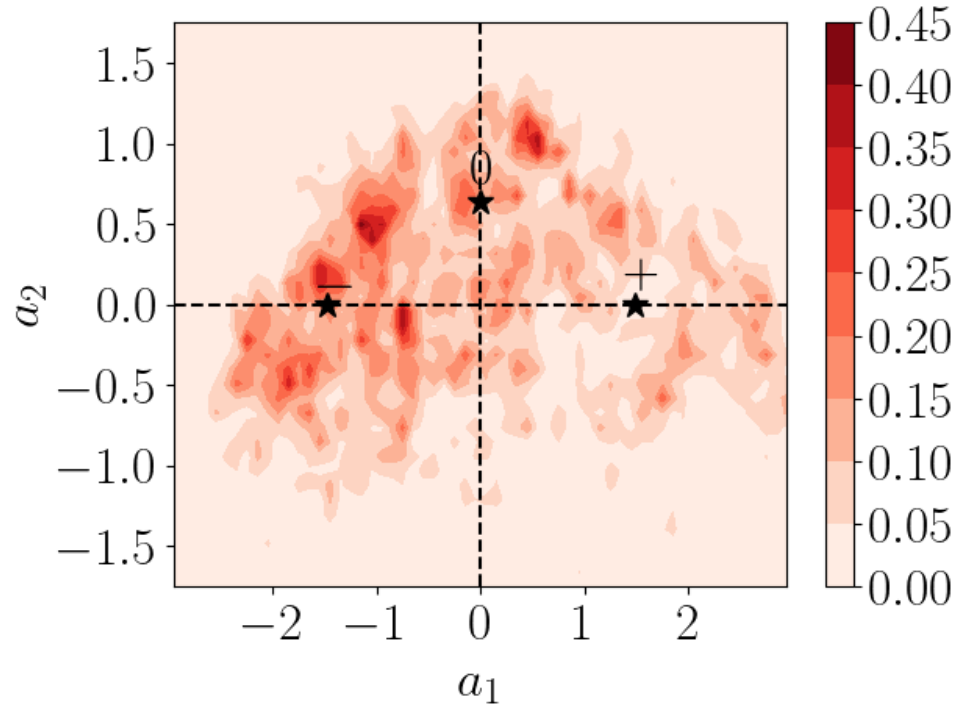


Fig. 16 Joint histogram of the POD amplitudes a_1 and a_2 at $AoA = 15^\circ$ and $Re = 3.4 \times 10^6$. The black stars correspond to the characteristic values used in figure 17.

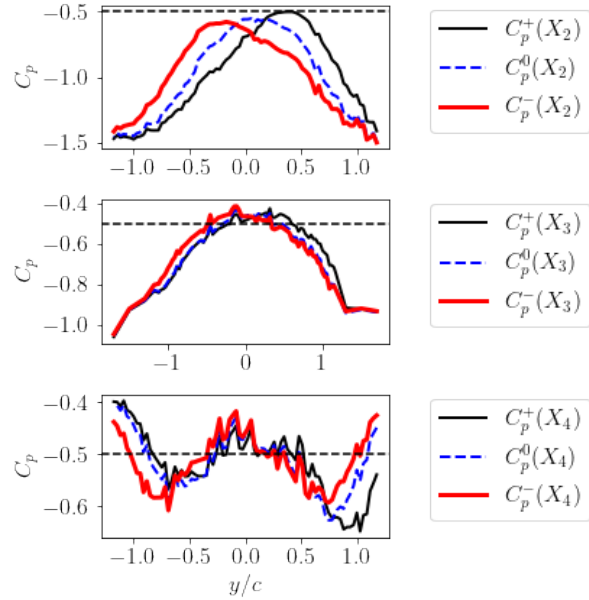


Fig. 17 Comparison of reconstructed signals based on the first two POD modes at $AoA = 15^\circ$ and $Re = 3.4 \times 10^6$.

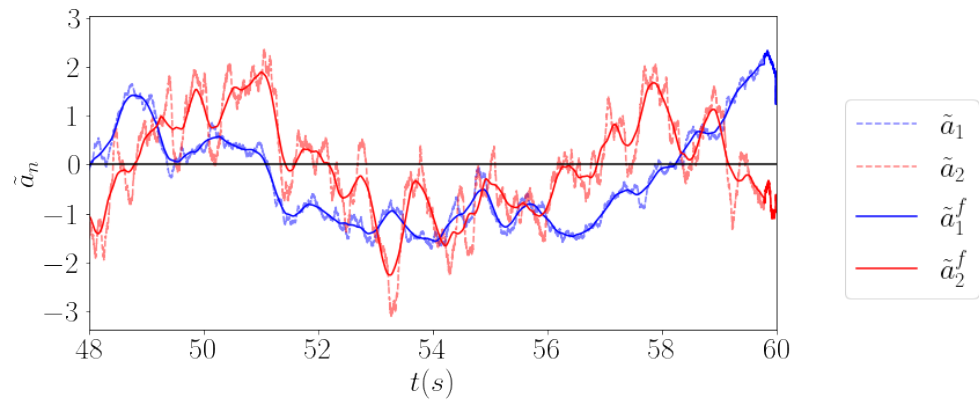


Fig. 18 Evolution of the normalized POD amplitudes \tilde{a}_1 and \tilde{a}_2 (dashed lines) at $AoA = 15^\circ$ and $Re = 3.4 \times 10^6$. The solid lines correspond to moving averages over 1 s.

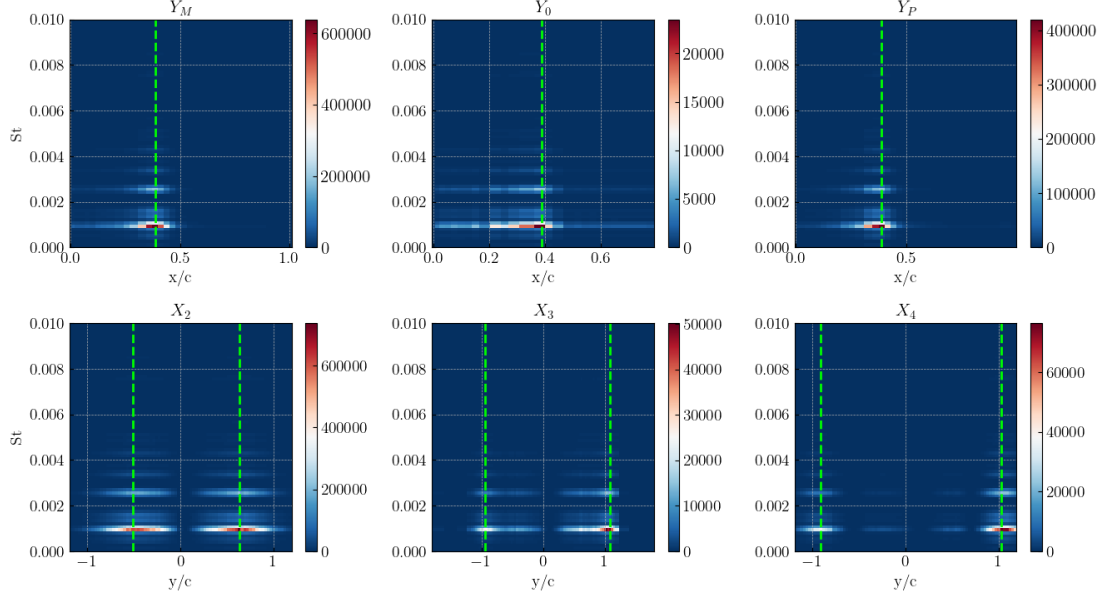


Fig. 19 Spectrogram of C_p projected onto the first POD mode at $AoA = 15^\circ$ and $Re = 3.4 \times 10^6$.

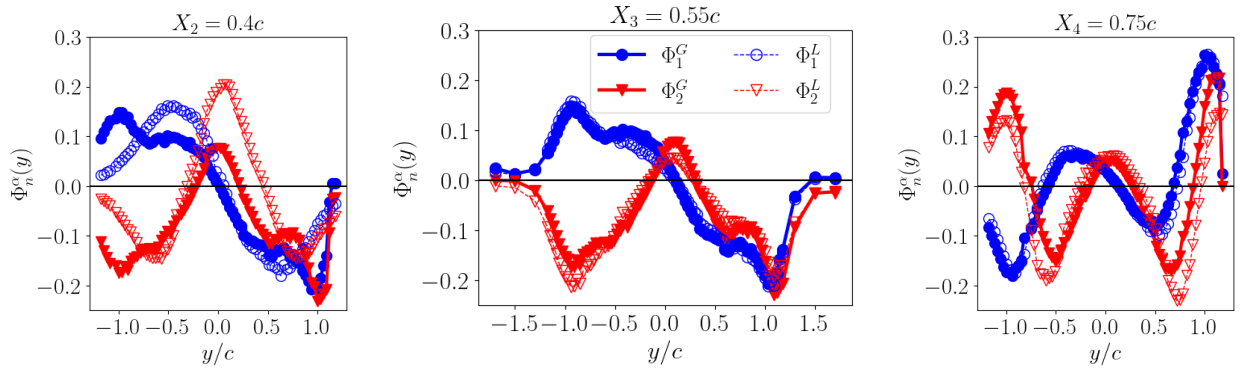


Fig. 20 Comparison of POD local modes with the local restriction of the global modes at $AoA = 15^\circ$ and $Re_c = 3.4 \times 10^6$. Full symbols: global POD modes; Open symbols: local POD modes.

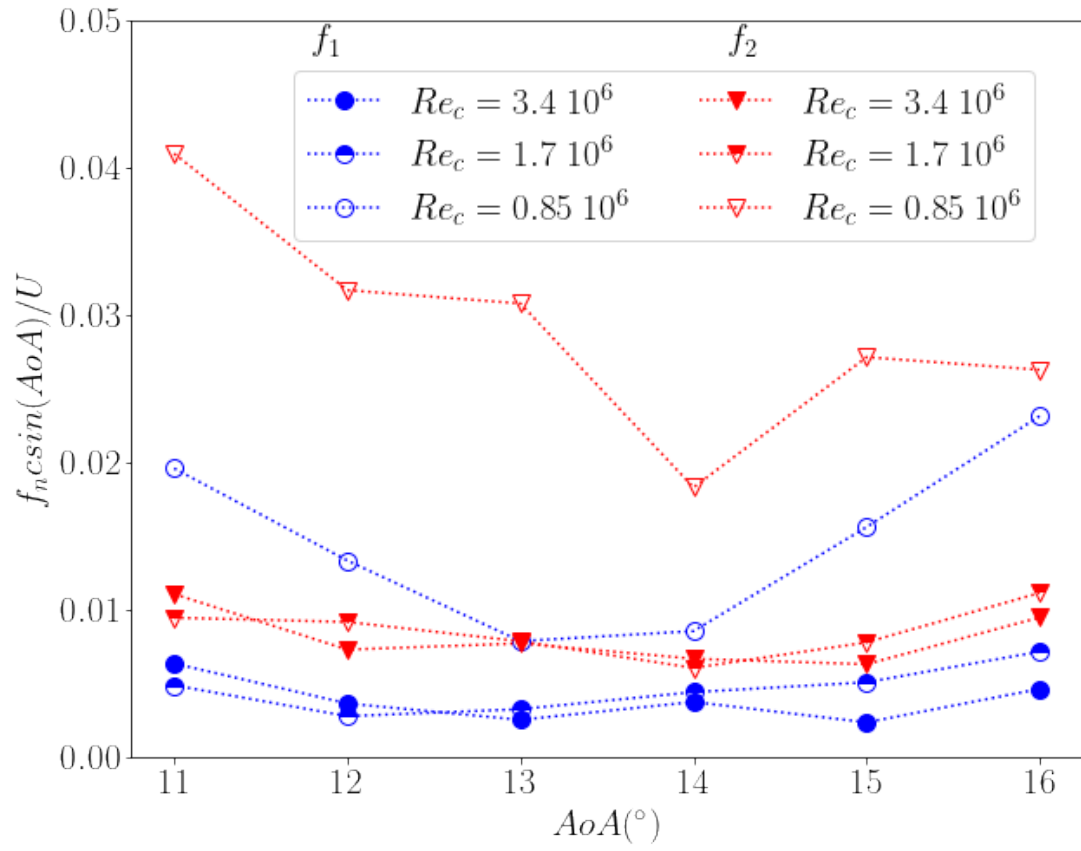


Fig. 21 Characteristic non-dimensional frequency f_n of the dominant POD amplitudes a_n for $n = 1$ (blue symbols) and $n = 2$ (red symbols).